Supporting Information

Supporting Information

Evidence that Sharp Interfaces Suppress Recombination in Thick Organic Solar Cells

Obaid Alqahtani[1,2], Seyed Mehrdad Hosseini[3], Thomas Ferron[4], Victor Murcia[1], Terry McAfee[4,5], Kevin Vixie[6], Fei Huang[7], Ardalan Armin[8], Safa Shoaee[3], and Brian A. Collins[1,4]*

[1]Materials Science and Engineering Program, Washington State University, Pullman, WA , 99164, USA.
[2]Department of Physics, Prince Sattam bin Abdulaziz University, Alkharj, 11942, KSA .
[3]Optoelectronics of Organic Semiconductors Institute, University of Potsdam, Potsdam-Golm, 14476, Germany.
[4]Department of Physics and Astronomy, Washington State University, Pullman, WA 99164, USA.
[5]Advanced Light Source, Lawrence Berkeley National Laboratory, Berkeley, CA 94720, USA.
[6]Department of Mathematics, Washington State University, Pullman, WA 99164, USA.
[7]Institute of Polymer Optoelectronic Materials and Devices, State Key Laboratory of Luminescent Materials and Devices, South China University of Technology, Guangzhou 510640, P. R. China.
[8]Department of Physics, Swansea University, Singleton Park, Swansea, Wales SA2 8PP, UK.

* Correspondence to brian.collins@wsu.edu

Table of Contents

S 1. Absorbance and J-V Characteristic Curves: Thickness Comparison

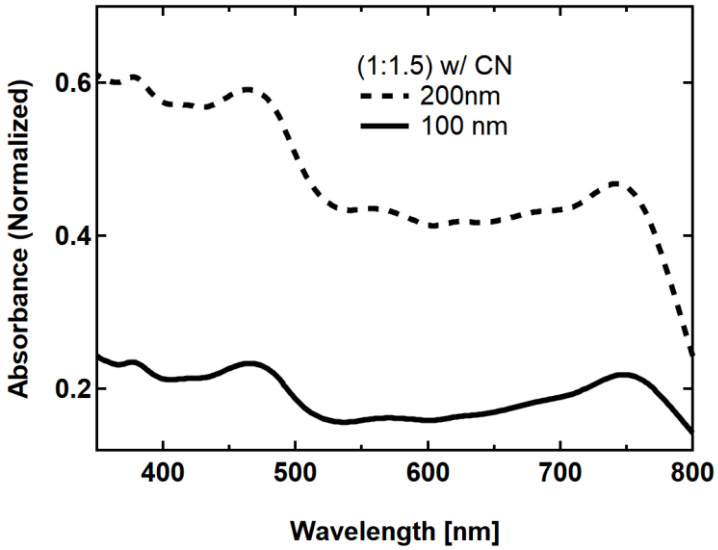

Figure S 1: UV-Vis absorbance for 1:1.5 with CN blends for comparison of 100 nm thick (solid) vs. 200 nm thick films (dashed).

Blend (NT812:PC71BM)	Additive CN [%]	V_{OC} [V]	J_{SC} [mA.cm^{-2}]	FF [%]	PCE (avg) [%]
(1:1.5)	0.5	0.75	14.8	70.4	7.9
(1:1.5) (thin)	0.5	0.76	13.7	73.2	7.5

Table S 1: Device performance summary for 1:1.5 blends with CN, at different thickness. Thick blend ~ 200 nm and thin blend ~ 100 nm.

S 2. Reduction Factors of Bimolecular Recombination

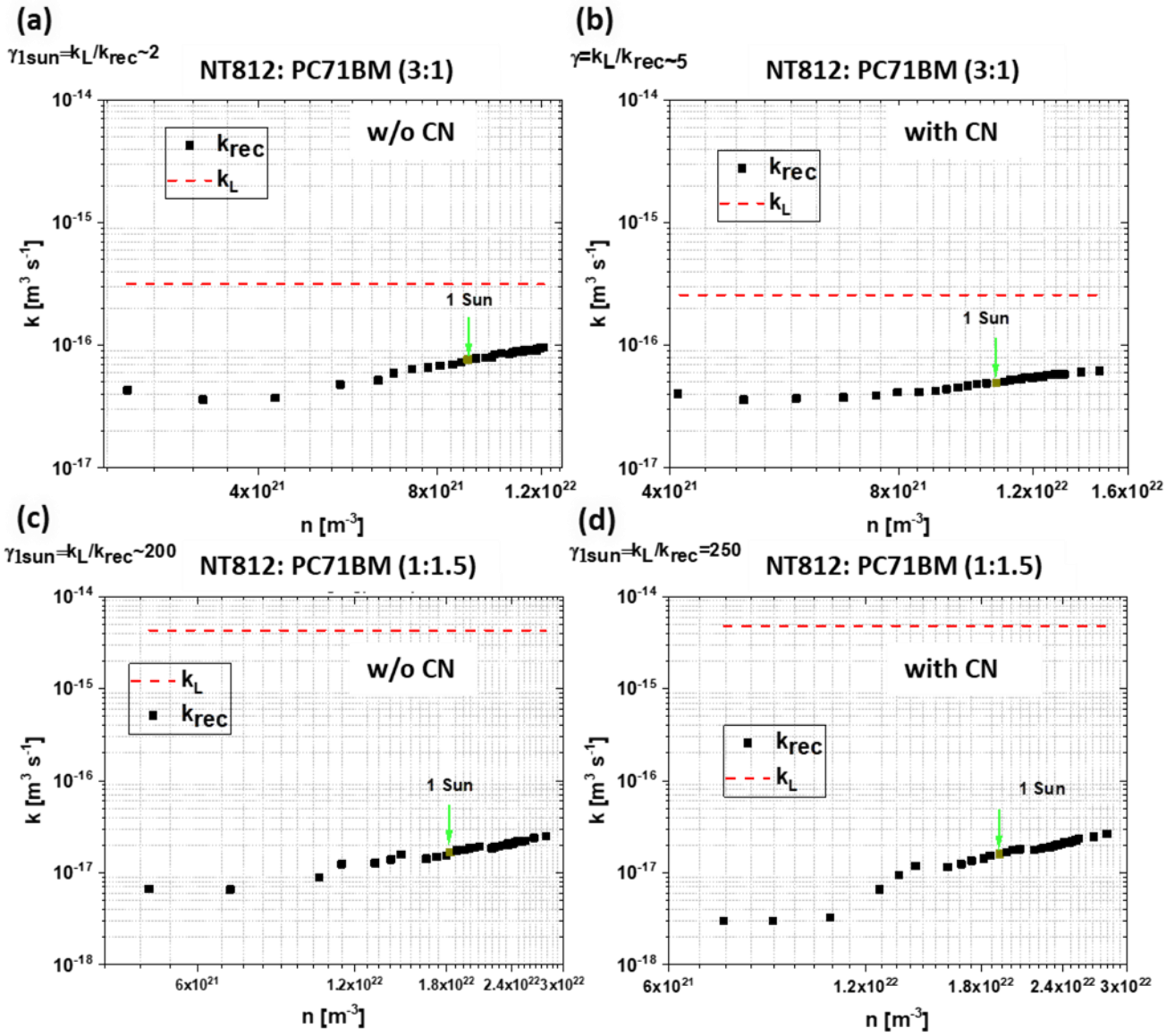

Figure S 2: Coefficient of bimolecular recombination as a function of carrier intensity in all four NT812:PC71BM blends. Calculated via steady-state bias-assisted charge extraction measurements, k_{rec} shown as black squares. The predicted Langevin recombination coefficient k_L is shown as dashed red lines. a) for NT812:PC71BM (3:1) blend without CN. b) for NT812:PC71BM (3:1) blend with CN. c) for NT812:PC71BM (1:1.5) blend without CN. d) for NT812:PC71BM (1:1.5) blend with CN.

See previous work for more experimental details and calculations about the coefficients of bimolecular recombination and charge carrier mobility. [2,3] Also, refer to the experimental section in the main text.

S 3. Charge Carrier Mobilities

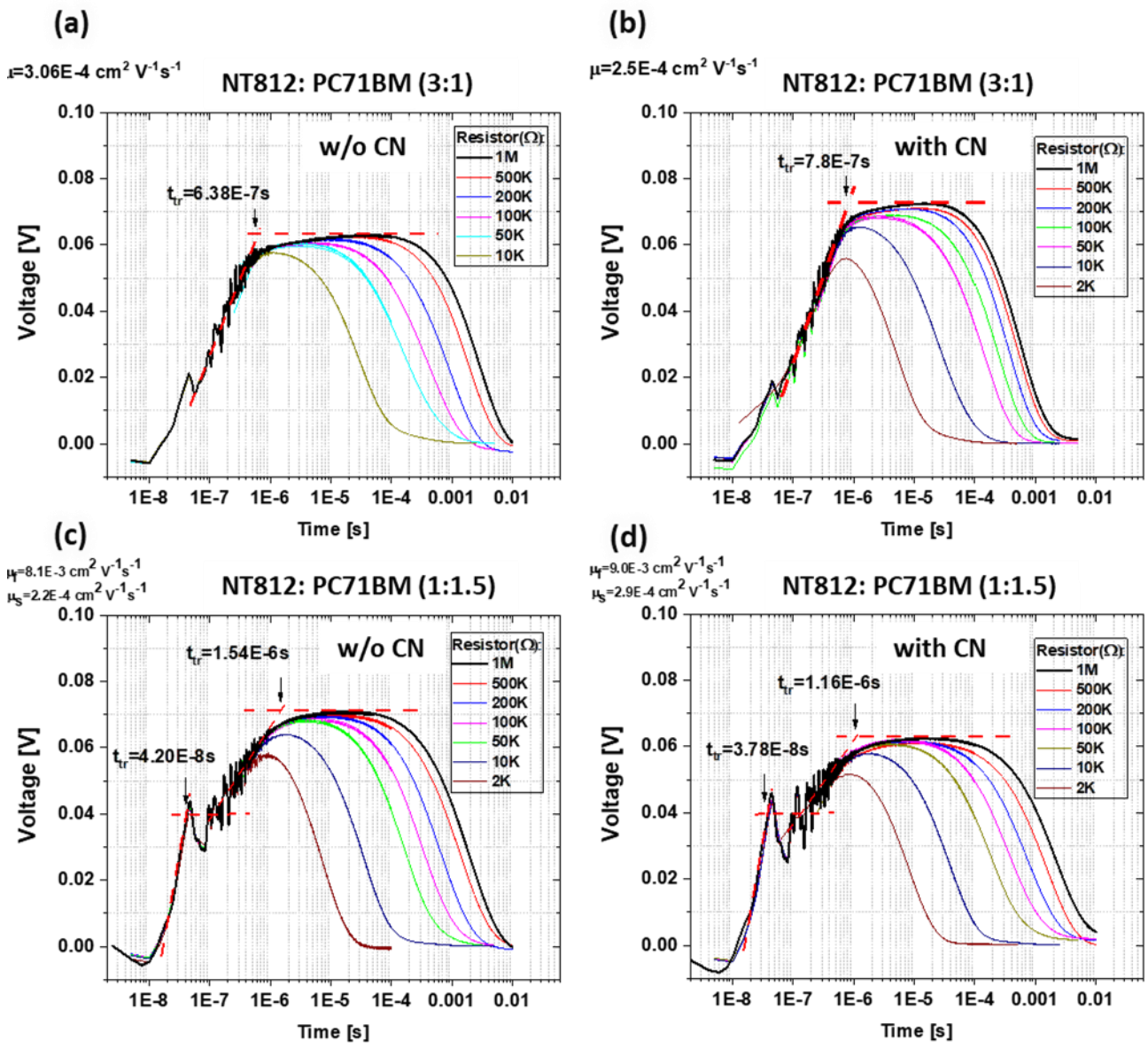

Figure S 3: Charge carrier mobilities were calculated via resistance-dependent photovoltage (RPV) transient measurements in all four blends of NT812:PC71BM with active layer thickness~ 200 nm. a) for NT812:PC71BM (3:1) blend without CN. b) for NT812:PC71BM (3:1) blend with CN. c) for NT812:PC71BM (1:1.5) blend without CN. d) for NT812:PC71BM (1:1.5) blend with CN.

S 4. GIWAXS Results and Analysis

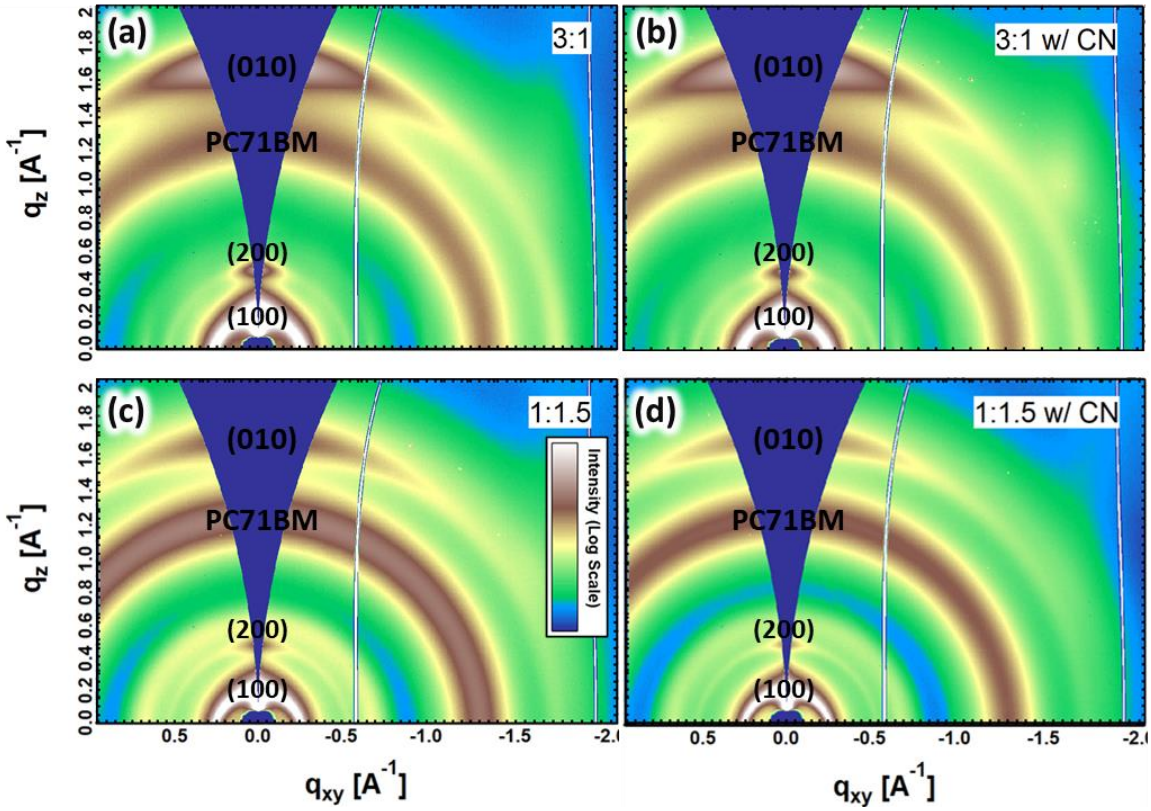

Figure S 4: 2D GIWAXS results for all blends as the labels indicate. All blends show PC71BM ring at q= 1.36 A^{-1} and pi stacking (010) of the polymer at q= 1.83 A^{-1}. The pi stacking shows stronger OoP signal meaning face-on preferential pi packing in face-on orientation with respect to the substrate. The 2D images are plotted with an arbitrary color scale of the scattering intensities, also corrected for the missing wedge a) for NT812:PC71BM (3:1) blend without CN. b) for NT812:PC71BM (3:1) blend with CN. c) for NT812:PC71BM (1:1.5) blend without CN. d) for NT812:PC71BM (1:1.5) blend with CN.

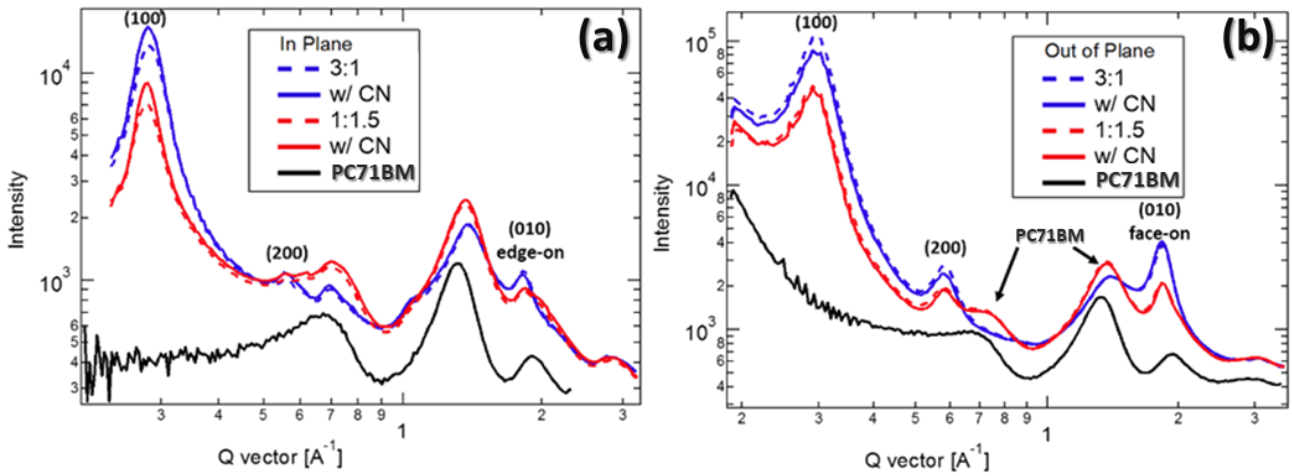

Figure S 5: 1D GIWAXS profiles extracted from 2D GIWAXS results in Figure S4. Additionally, 1D profiles for neat PC71BM are included as reference for peak assignments. a) Profiles taking in the horizontal sector, i.e. in plane (IP). (b) Profiles taking in the vertical sector, i.e. out of plane (OoP).

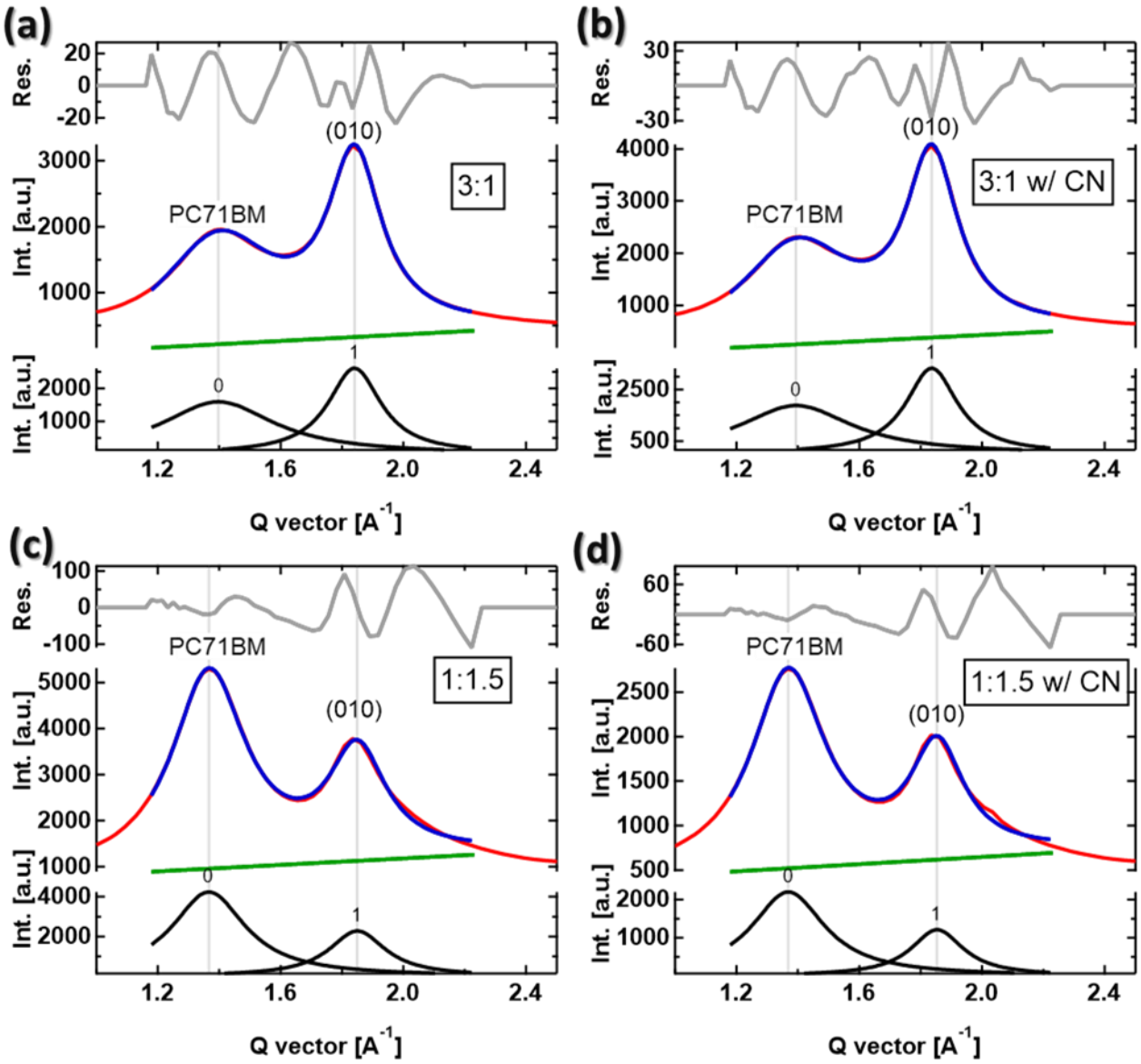

Figure S 6: 1D OoP GIWAXS data (red) were fitted with multi-peak fitting (blue) for PC71BM peak (at q=1.36 A^{-1}) and pi stacking face-on peak (010) for the polymer (at q=1.83 A^{-1}). Each peak was fitted to a Lorentzian with a linear background (green). FWHM values from the fitting results (black) were inserted in Scherrer equation [$D = \frac{2\pi K}{FWHM}$, $K\ (constant) = 0.94$] to calculate the corresponding coherence length (D) for the real-space molecular packing and ordering that causes those scattering peaks. a) for NT812:PC71BM (3:1) blend without CN. b) for NT812:PC71BM (3:1) blend with CN. c) for NT812:PC71BM (1:1.5) blend without CN. d) for NT812:PC71BM (1:1.5) blend with CN.

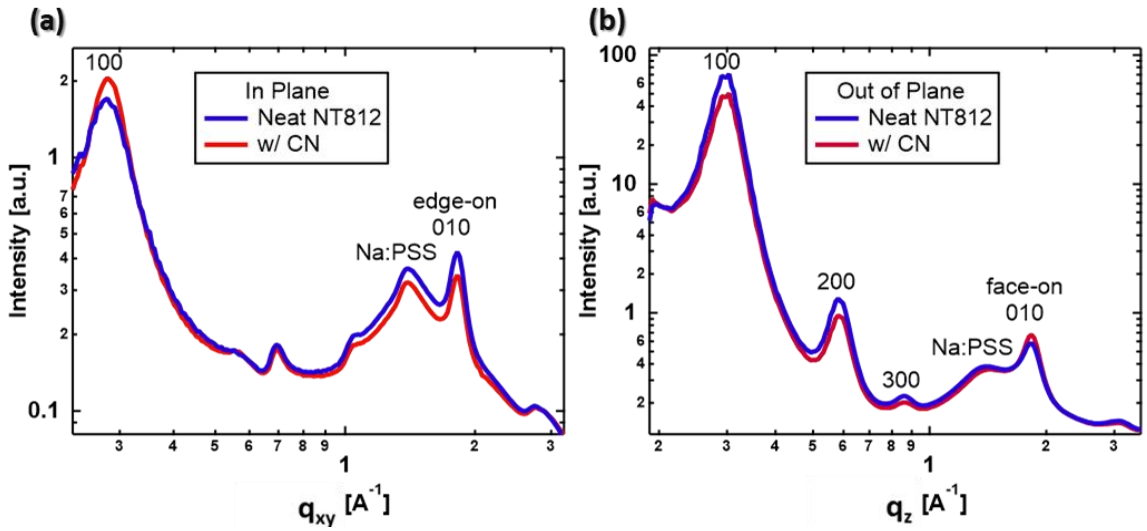

Figure S 7: 1D GIWAXS profiles for neat polymer (NT812) spin casted on Na:PSS/Si substrates from solution with and without additive CN. a) 1D profiles for the IP direction. b) 1D profiles for the OoP direction.

Parameter	Peak position		d-spacing	
Peak\Sector	In Plane [Å^{-1}]	Out of Plane [Å^{-1}]	In Plane [Å^{-1}]	Out of Plane [Å^{-1}]
Lamellar (100)	0.28	0.29	22.44	21.67
Pi Stacking (010)	1.83 (edge-one)	1.83 (face-on)	3.43	3.43

Table S 2: Molecular packing details extracted from GIWAXS data. Scattering peak positions and d-spacing ($d = \frac{2\pi}{Q}$) for pi stacking (010) peaks and their corresponding lamellar (100) peaks of NT812 in pure polymer films and in blends with and without solvent additive CN. Also, the orientation of pi stacking with respect to substrate was indicated in parentheses. Note: those peck positions and d-spacing values do not change in all samples (both in neat polymer and blend films) which indicates that similar packing and ordering in neat polymer exist in blends.

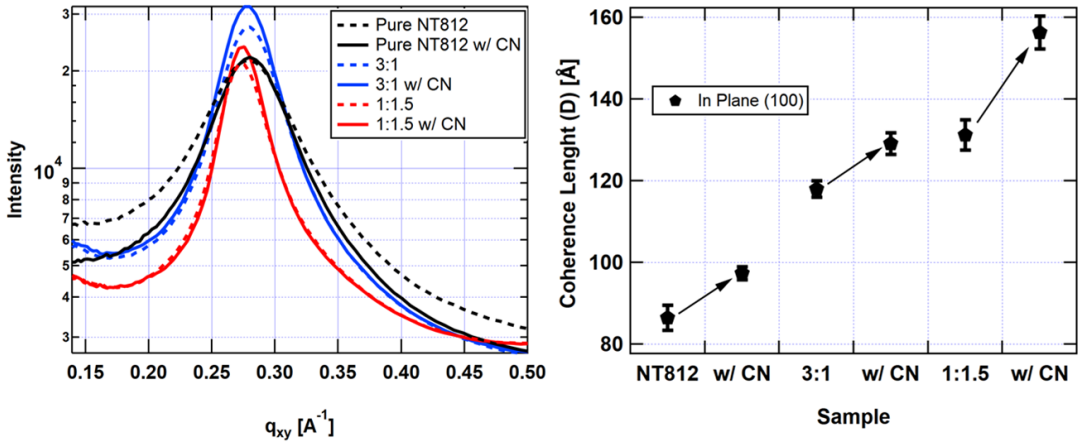

Figure S 8: In plane GIWAXS profiles for all blends and neat films with and without CN (left) for (100) peak. Right: coherence length (D) for the in-plane lamellar peaks (100) that are presented on the left side.

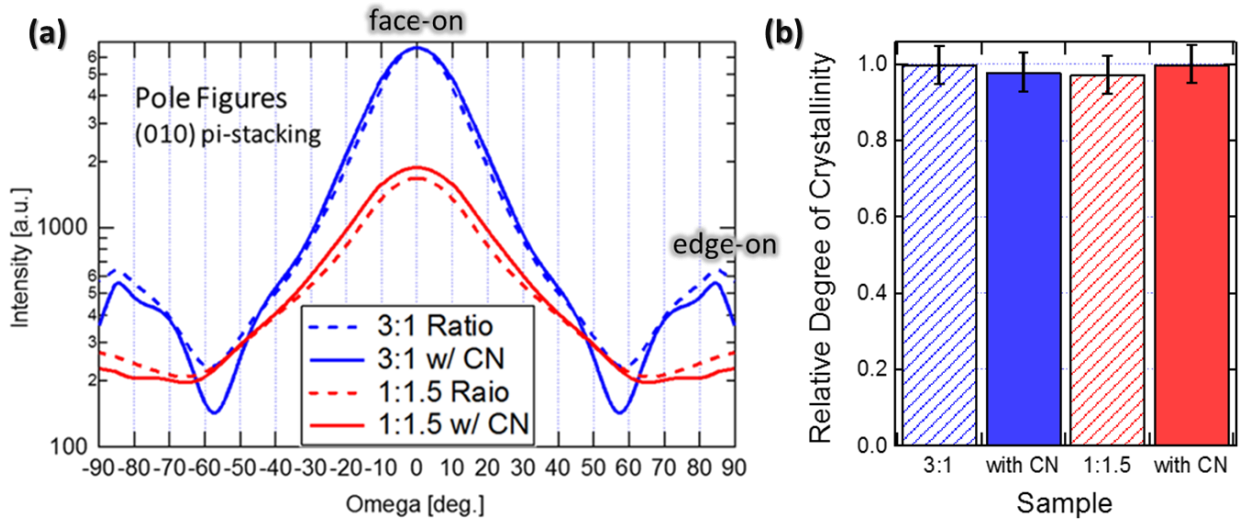

Figure S 9: a) Pole figures for NT812 (010) pi-stacking were processed for all blends from GIWAXS data. Where "Omega" defines the angle between the crystallite orientation and the surface of the substrate. b) Bar graph representation of relative degree of crystallinity (rDoC) for (010) pi-stacking in all NT812: PC71BM blends, calculate by integrating the profiles in part (a).

Pole figures,[4] here, describe orientation distribution of the polymer π-π stacking (010). Thus, the results suggest that all blends show that NT812 prefer (face-on) orientation with respect to the substrate. Relative degree of crystallinity (rDoC) analysis for (010) pi-stacking show that all blends have similar rDoC for the π-π stacking (010) peak in the polymer domains.

$$rDoC = \frac{Volume\ of\ Polymer\ Crystal\ (all\ orientations)}{Total\ Volume\ of\ Polymer}$$

S 5. Near-Edge X-Ray Absorption Fine-Structure (NEXAFS) Spectroscopy

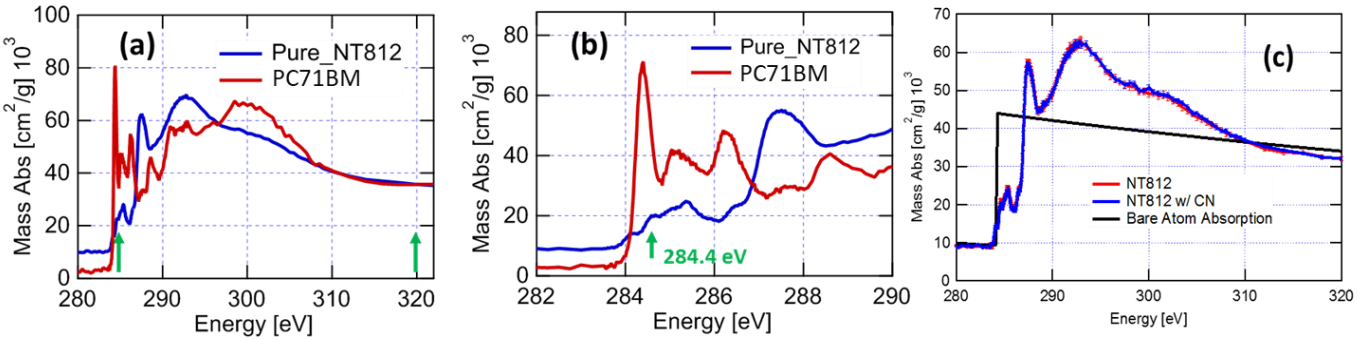

Figure S 10: a) NEXAFS spectra for pure NT812 and pure PC71BM scaled to their bare atom absorption coefficient. The STXM imaging energies were selected based on those NEXAFS spectra, mass absorbance, for the donor and acceptor. b) A zoomed in version of (a). At 284.4 eV, the fullerene has higher absorbance than the polymer. Another imaging energy was chosen to be 320 eV where the fullerene and polymer absorb about the same. c) NEXAFS spectra for pure polymer with and without solvent additive CN as shown in (c). The mass absorbance is relatively similar for neat polymer (NT812) with and without CN.

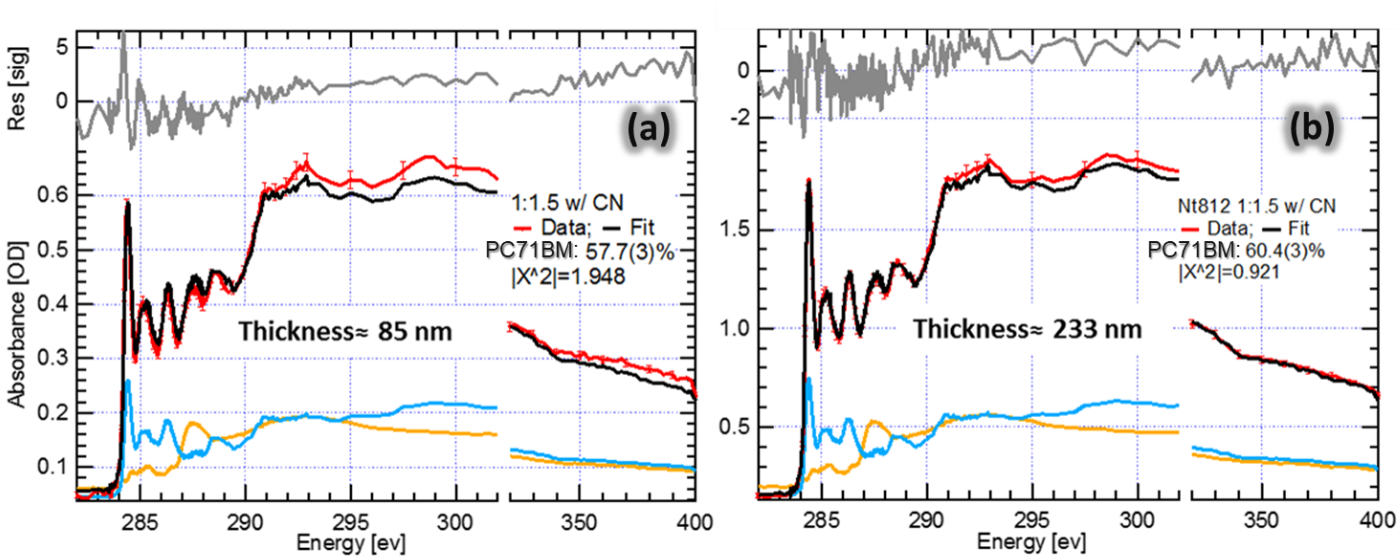

Figure S 11: NEXAFS for NT812: PC71BM (1:1.5) blends (red) with CN, but different thicknesses. Linear fits (black) of the NEXAFS spectra of the blend films (red) with reference NEXAFS spectra for neat materials, NT812 (orange) and PC71BM (blue). The fitting of NEXAFS spectra for blend films enables quantitative determination of average chemical composition. The film thickness also calculated from beer-lambert law. The fit residuals shown on top (gray). Results show that the average composition of both blends ~ 60% PC71BM, which agree with the blending weight ratio (1:1.5). a) for a thin NT812:PC71BM (1:1.5) blend with CN. b) for a thick NT812:PC71BM (1:1.5) blend with CN

S 6. Scanning Transmission X-ray Microscopy (STXM) for Composition Mapping

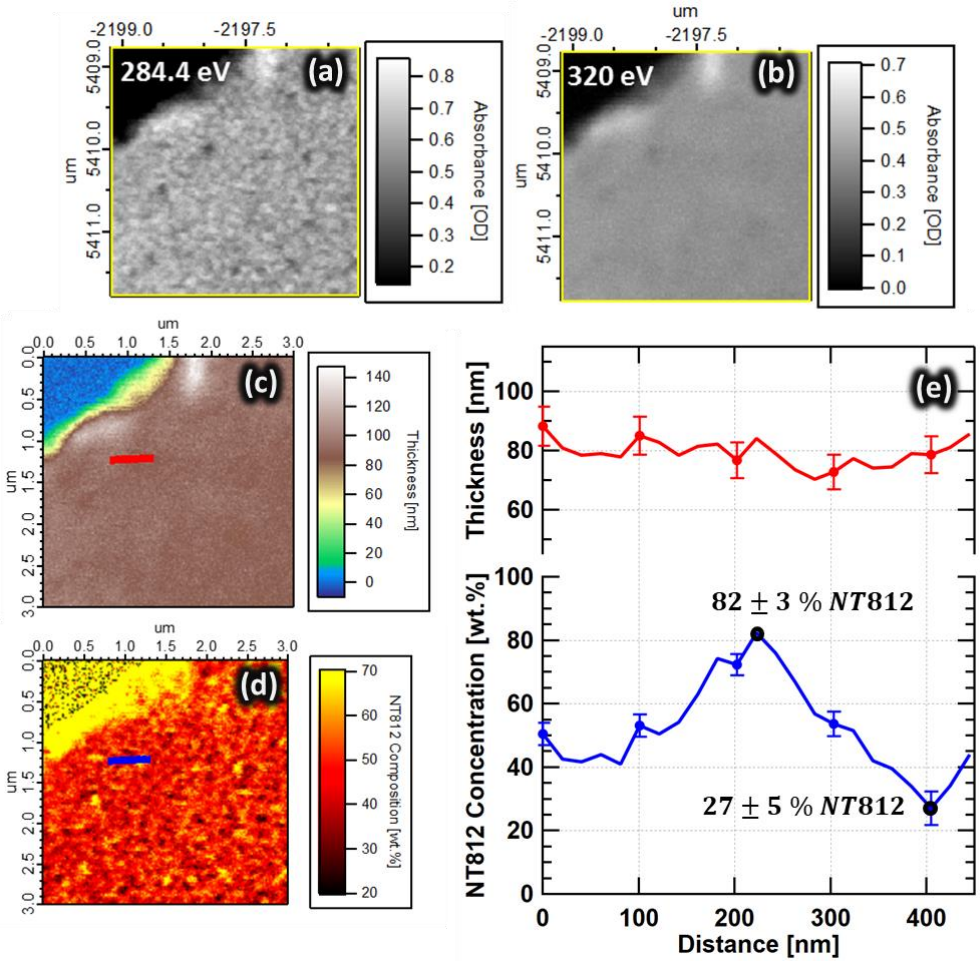

Figure S 12: Composition mapping analysis for a thin NT812: PC71BM (1:1.5) blend with CN. a) A STXM image was taking at fullerene resonant energy (284.4 eV) and the image in (b) was taken at a non-resonant energy (320 eV). By combining those STXM images with NEXAFS spectra for neat materials, a thickness map (c) as well as a composition map (d) were generated. e) Line profiles show variation in thickness (Red) and composition (blue) across a region of the blend film as presented in colored lines in c and d. From (e) the average thickness is about 85 nm. Also, the polymer concentration in the polymer-rich domain is 82 ± 3 wt. % and 27± 5 wt. % in the fullerene rich domain. The deconvolution of the X-ray beam tails suggests pure domains (see Figure S 13-15 for the deconvolution analysis).

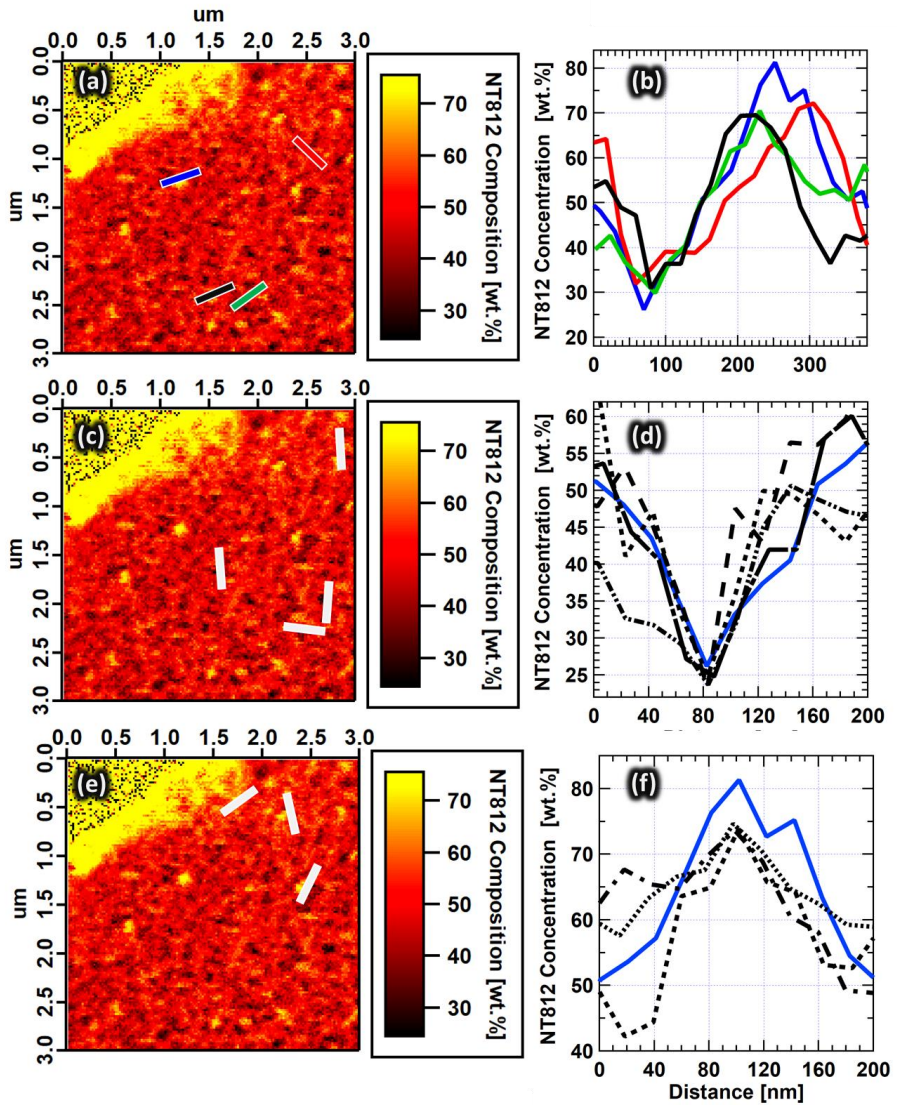

Figure S 13: The composition images on the left, a, c and e are the same composition image as in Figure S 12 d with bars that correspond to the spots where the 1D line profiles in b, d and f were extracted from. b). Shows 1D concentration profiles the were extracted from different spots as indicated with colored lines in (a). The general trends of feature size and compositional fluctuation are consistent across the film. d). The profiles were extracted from fullerene-rich spots, as indicated with white bars in (c), to show that the polymer concentration gets as low as 25% or less. f). Concentration 1D profiles extracted from (e) as indicated by white bars to show that the polymer concentration can got above 75%. The blue traces in d and f are the same as the blue one in b. In general, the polymer concentration fluctuation, high and low, can be found in several spots of the film. It was impossible to get 100% or 0% polymer concentration profiles from the raw compositional maps due to the x-ray beam convolution with the relatively small domain sizes in those NT812: PC71BM systems. Therefore, 1D and 2D deconvolution analyses were conducted to retrieve the real molecular concentration in the polymer and fullerene domains.

After considering the convolution of the x-ray beam tails with film domains, the results suggest the presence of pure polymer and fullerene domains. The deconvolution analysis of the line profiles is similar to our previously published calculation.[5] We have also conducted 2D deconvolution analysis as shown in Figure S14 and S15. Our 2D deconvolution results also suggest the existence of pure polymer and fullerene domains.

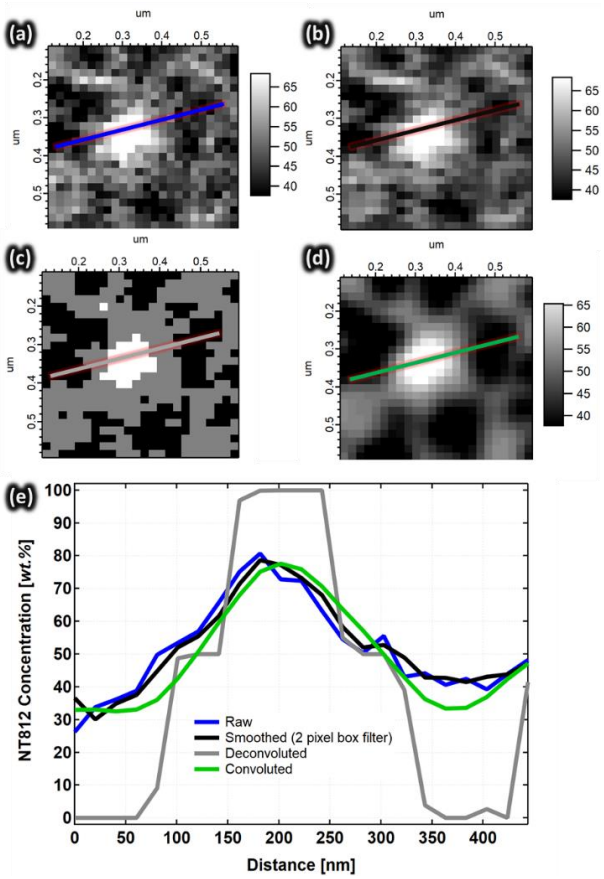

Figure S 14: a). This is the same image as the raw composition map in Figure S 12d but zoomed in on the spot where the blue line is, also in a grays color scale instead. b). A smoothed version of the image in (a), smoothed with a 2-pixel box filter to reduce the noise effects. c). A deconvoluted image that shows better representation of the real film. Where black is 100% fullerene, gray is 50% and white is 100% polymer. The gray regions, i.e., 50% concentration, indicate film spots where there are vertical overlaps between pure polymer and fullerene domains. d). A result of convolving (c) with the X-ray beam profile in Figure S 15. e). 1D line profiles to compare compositional variation across different domains in the 2D images, a, b, c and d (as indicated by colored lines in the images).

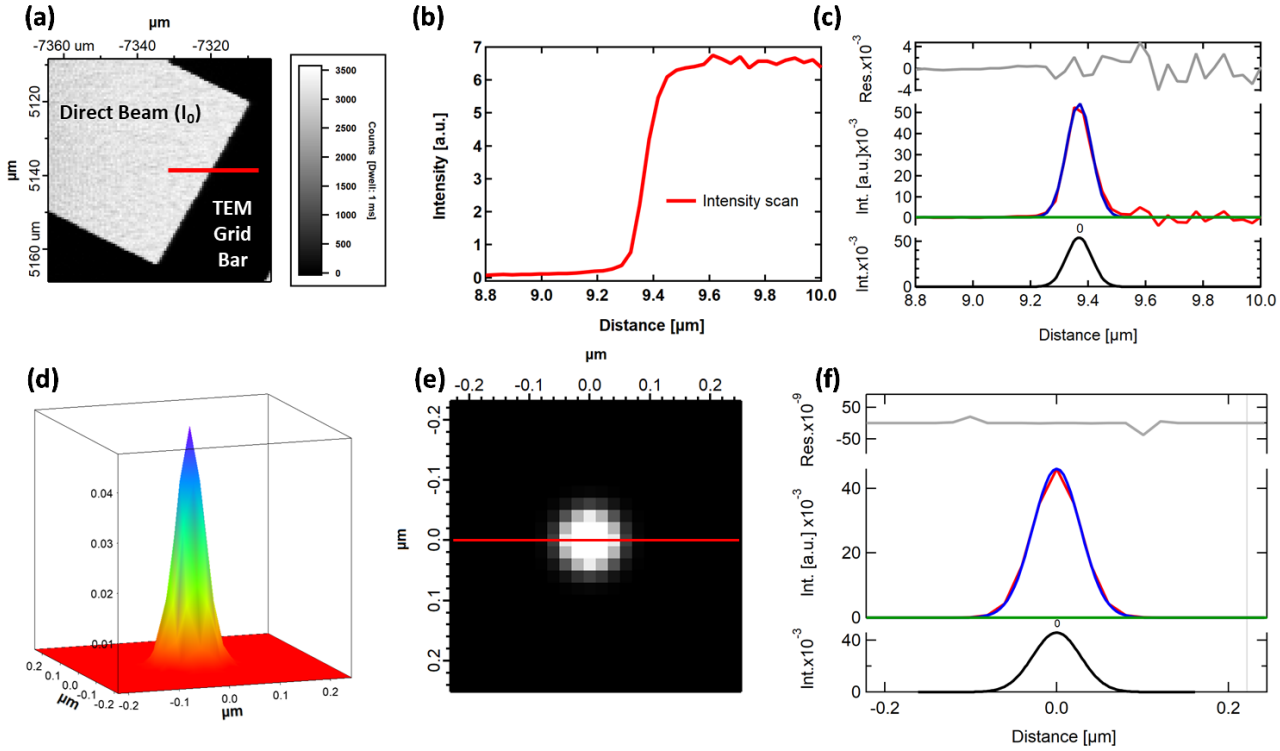

Figure S 15: Constructing a 3D representation of the X-ray beam profile. A scan across a TEM grid bar "a knife-edge scan" was taken as shown in (a). The dark regions show the grid bars where the beam is totally blocked. The bright region is the direct beam through a mesh hole. b) An intensity scan across a knife edge of the TEM grid bar as indicated by a red line in (a). The total intensity changes from zero "dark", where the beam is totally blocked, to direct beam (I_0). The intensity line scan was taken at E = 320 eV. c) A gaussian peak fitting of the derivative (red) of the intensity line scan in b. The FWHM is ~ 100 nm, which should be the maximum beam FWHM because the beam was not 100% focused. d) An approximate 3D representation of the X-ray beam, assuming a gaussian symmetric beam. e) A 2D representation of (d). f). A peak fitting for a line profile that was extracted from (e), as indicated with a red line.The fitting results suggest a gaussian beam profile with FWHM~ 65 nm.

The knife-edge measurement of the STXM X-ray beam is simple, yet useful to get a good approximation of the beam width and its upper limit. Our calculation of beam profile width (FWHM~ 100 nm) shows similar or even sharper beam than previous calculations (FWHM>100 nm).[6]

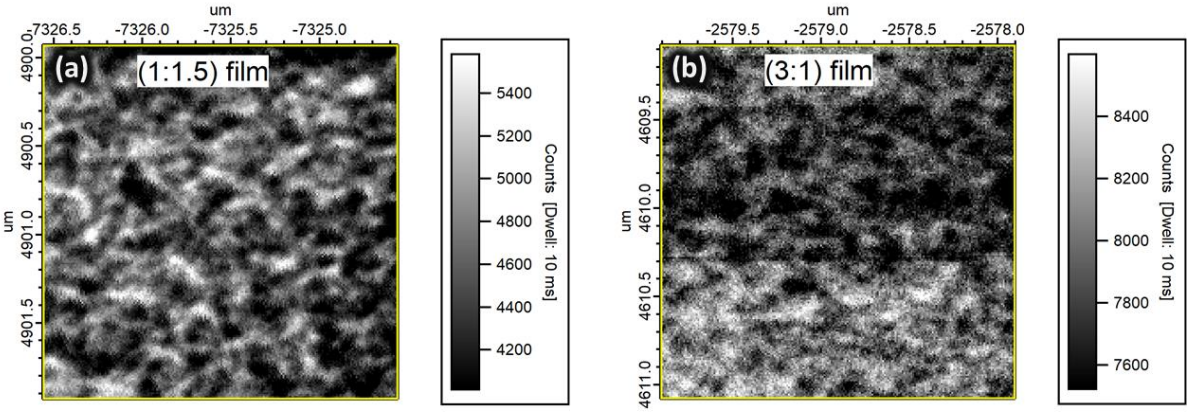

Figure S 16: STXM composition scans were taken on ~ 200 nm films at 284.4 eV, which is fullerene absorption peak, i.e., a fullerene resonant energy. PC71BM (dark regions) and NT812 (white fibrils). The images are for a 1:1.5 blend without CN% (a) and a 3:1 blend with 0.5 CN% (b). The overall shapes of PC71BM domains and polymer fibrils in the thick (1:1.5) film is similar to the thin film (see Figure 3b in the main text).

S 7. Materials Contrast: X-ray Scattering Energy Selection

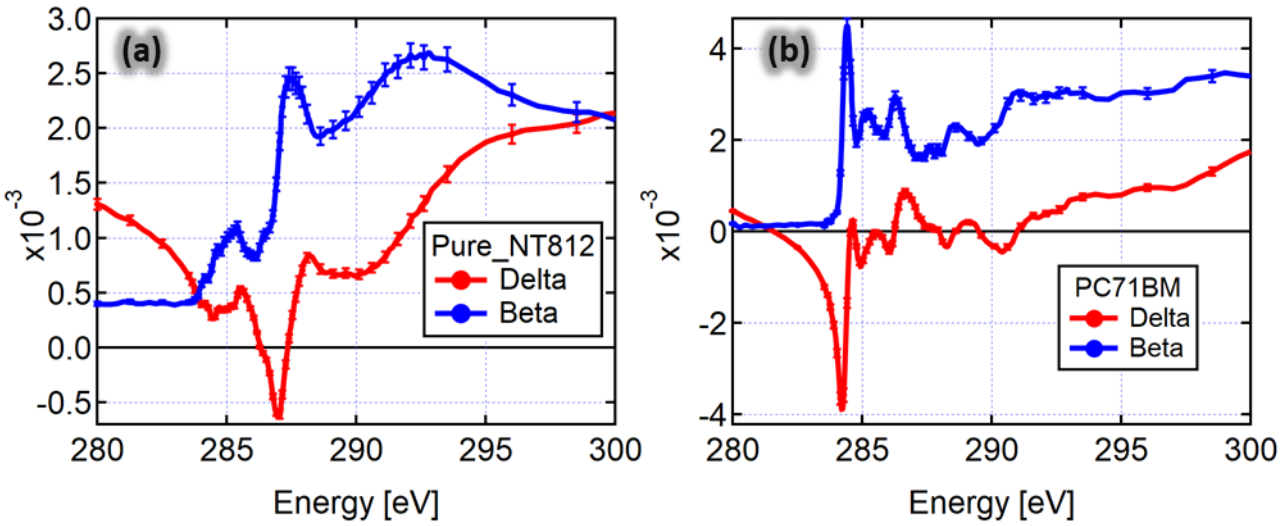

Figure S 17: Scattering intensity (I) is proportional to the contrast function, I(E) $\propto|\boldsymbol{\Delta n}|^{\mathbf{2}}$, where (n) is index of refraction $\boldsymbol{n = 1 - \delta + i\beta}$. The imaginary part (beta) is related to absorbance, calculated from NEXAFS measurements, and the real part (delta) is calculated from the Kramers Kronig transform. The graphs show the real (red) and imaginary (blue) parts of indices of refraction for neat polymer (a) and neat fullerene (b).

Details of the Kramers Kroning Transform can be found elsewhere.[7]

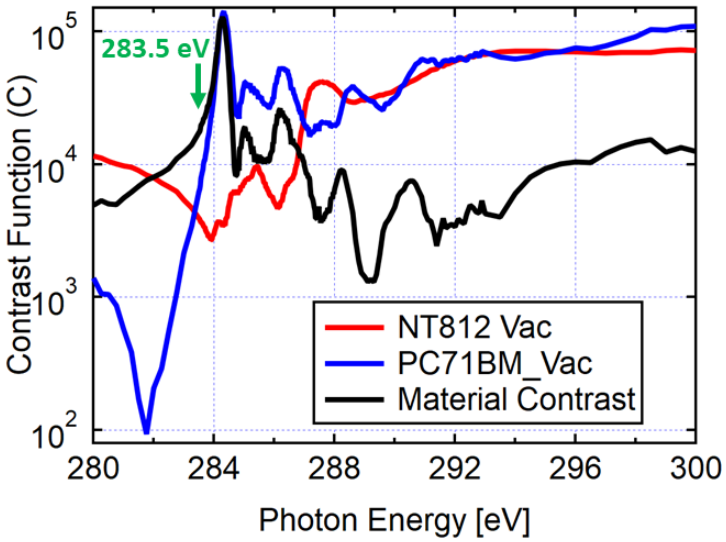

Figure S 18: Materials and vacuum contrast functions based on the material indices of refraction, where contrast function is $C = E^2|\boldsymbol{\Delta n}|^{\mathbf{2}}$.

See previous work for more details on this transformation and calculation of index of refraction and contrast function.[8]

S 8. RSoXS: Film Thickness Calculation via NEXAFS Absorbance Profiles

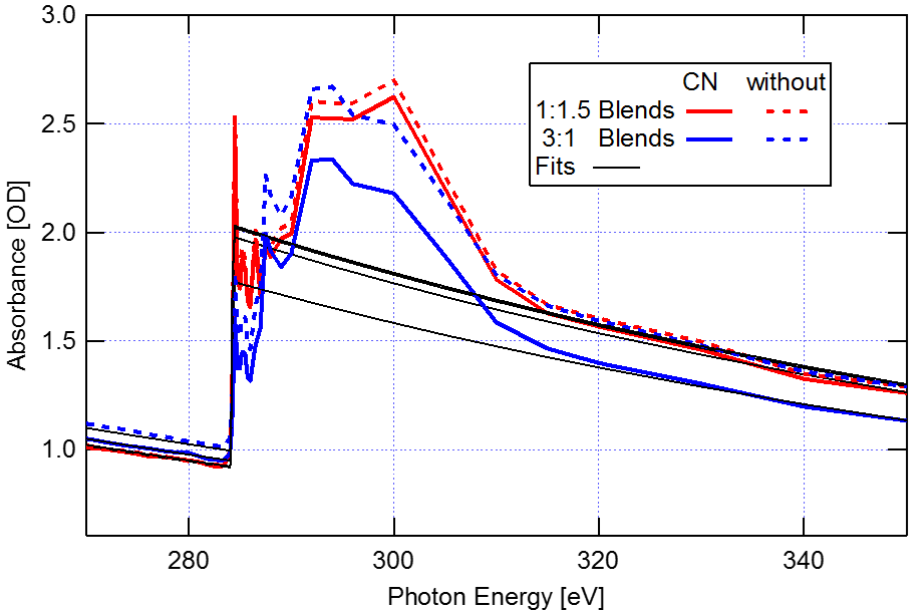

Figure S 19: NEXAFS measurements for all blends to determine film thickness at the same spots where RSoXS data was taken on each film. NEXAFS profiles were scaled to the mass absorbance coefficient (black fits) of the bare atoms. Film thickness calculated via Beer-lambert's law then used to normalize RSoXS data. Where $the\ film\ hickness = \frac{1}{\mu(E) \times \rho}\ ln\left(\frac{I_0(E)}{I(E)}\right)$, here $I_0(E)$ is the intensity of the direct incident beam, $I(E)$ is intensity of the transmitted beam through the film, $\mu(E)$ is the mass absorption coefficient, and ρ is the film density.

S 9. RSoXS: Composition Variation and Characteristic Length

Refer to our previous work, for more details about the two domain modeling and calculation of composition fluctuation.[5]

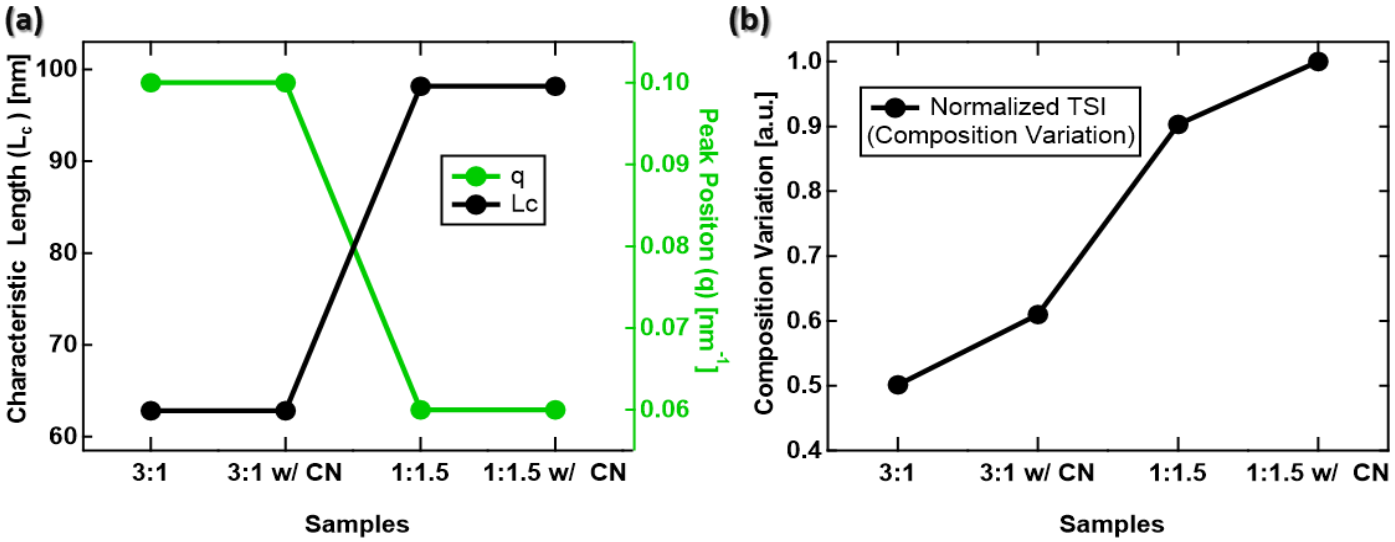

Figure S 20: Calculations based on RSoXS results in the main text (Figure 4a). a) Characteristic length (Lc) of the corresponding features (black) for each film was calculated as Lc=2π/q where q is the peak position (green). b) The composition variation in each blend was calculated by normalizing the total scattering intensity (TSI) values for each blend to TSI for 1:1.5 with CN, which shows the highest scattering intensity. The TSI~ integral of the RSoXS scattering profiles in Figure 4a of the main text.

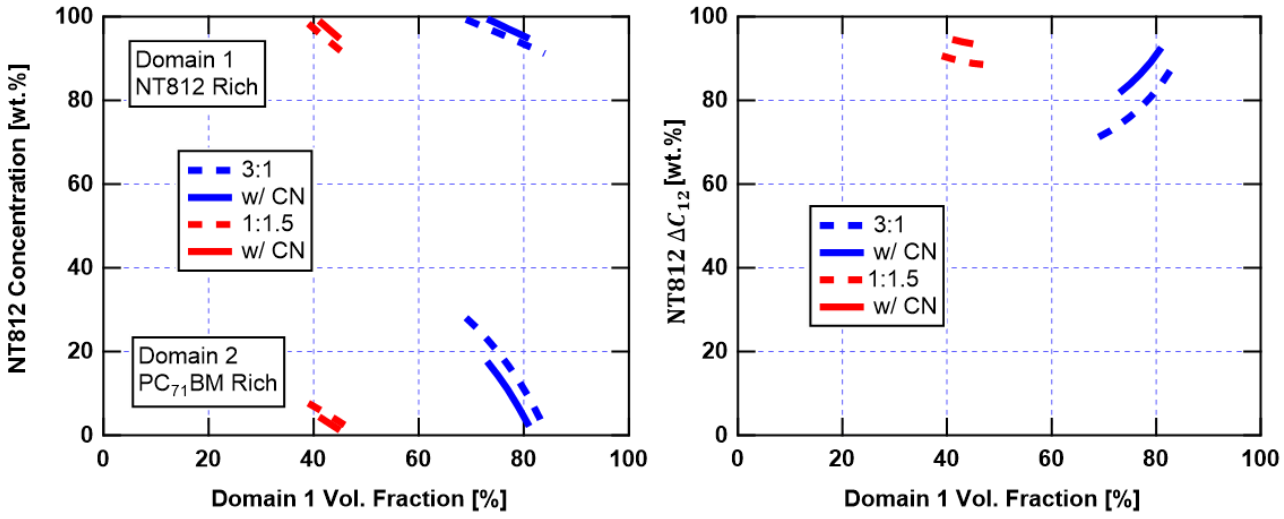

Figure S 21: a) Concentration variation of the polymer as a function of its volume fraction, based on two domains model. b) Composition fluctuation of the polymer between the two domains ($\Delta C_{12} = C_1 - C_2$) which indicates the lateral RMS of the polymer concentration in a film.

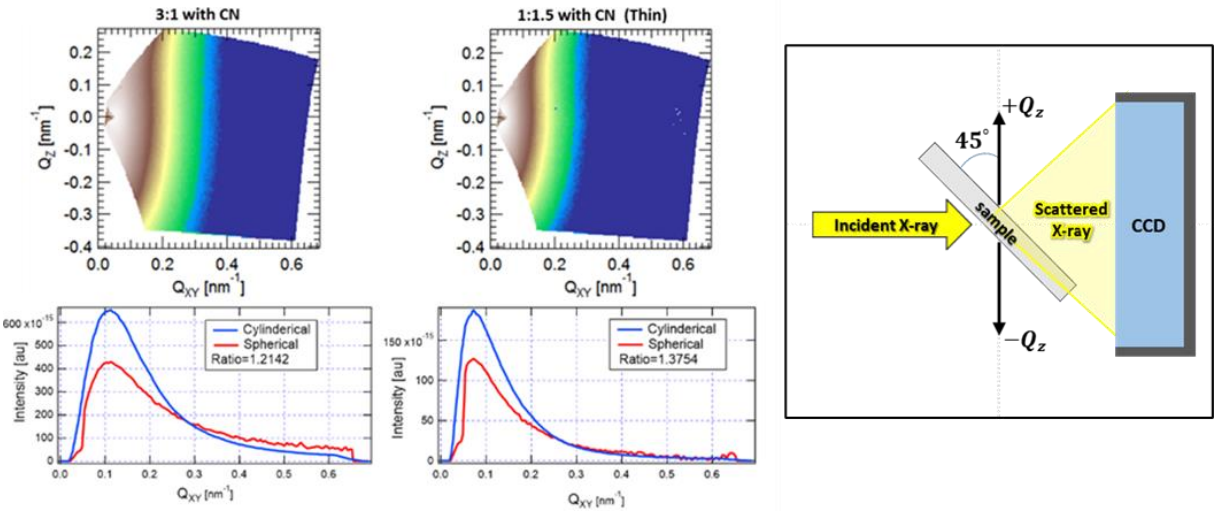

Figure S 22: RSoXS results at 45-degrees sample tilt plotted to explore the qz component. Data examples shown here are for the 3:1 (200 nm) film with CN and 1:1.5 (100 nm) film with CN. 2D RSoXS data shown in Qz vs Qxy (top) and extracted average 1D profiles (bottom). The intensity decreases in direction of -Qz due to higher absorption of photons that travel longer paths through the sample as shown in the 45-degee RSoXS geometry diagram on the right side.

The 2D data indicates that there are no features in the z-direction, i.e. no vertical stratification. The 1D profiles show features with peak positions that agree with RsoXS data at normal-intendance (refer to Figure 4a). For more details on the transmission scattering gemetery at 45-degrees of sample tilt, refere to our previous work.[9]

S 10. Donor-Acceptor Interfacial Width Calculation

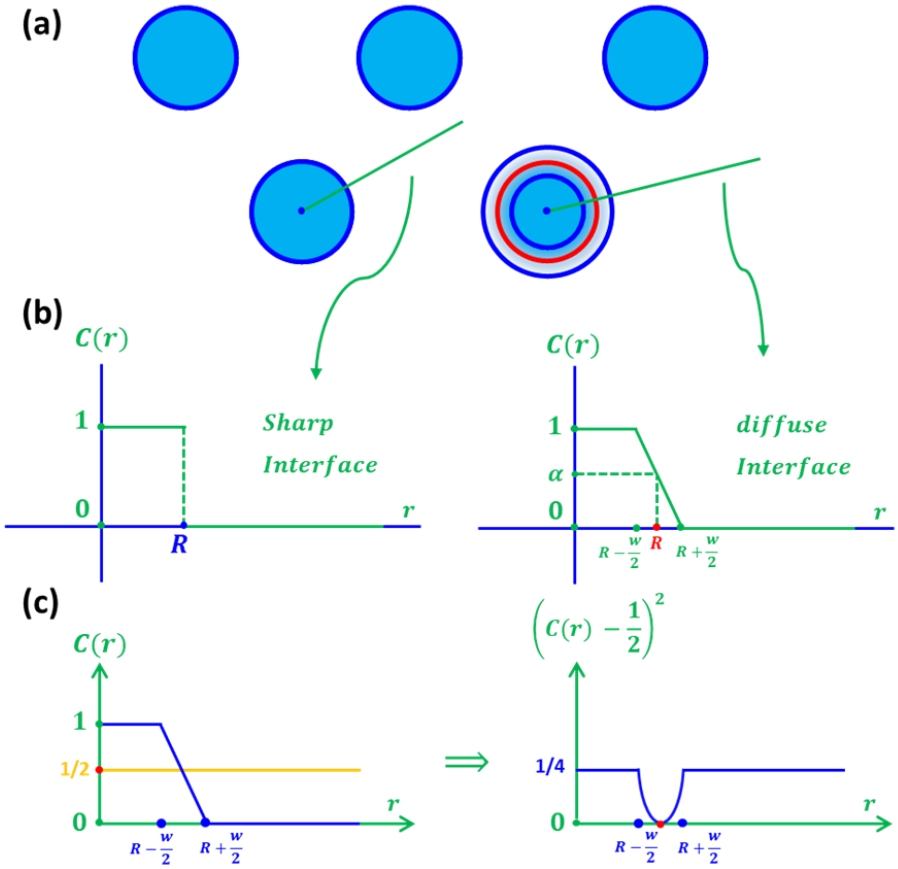

Figure S 23: Model to calculate interfacial width. a) Schematic of fibril cross-sections. b & c) composition profiles extracted from the green lines in (a).

RMS Composition Fluctuation Between Pure Domains Converted to Interfacial Width

To calculate the effects of molecular mixing between domains, we combine our measurement of the RMS composition fluctuation ΔC_{RMS}, and characteristic length L_C both from RSoXS analysis, and the known average polymer concentration in the blend $\alpha = \frac{m_p}{m_p + m_f}$. For the purposes of the calculation, we start with the assumption of a hexagonal lattice of pure cylindrical polymer fibrils in a matrix composed of pure fullerene (Figure S22a). However, later we show how we can relax the assumption of a lattice or regular fibril radii R. We assume that $L_C = d$ the domain spacing and can calculate the fibril radii using basic geometry

of the hexagonal lattice $R = d\sqrt{\frac{\sqrt{3}\alpha}{2\pi}}$. Taking the origin to be at the center of a cylindrically symmetric fibril, we can characterize the composition as a function of radius r in the sample $C(r)$ in the case of sharp interfaces and in the case of a linearly varying concentration over a region w as shown in Figure S22b. We can connect this model with our measurement ΔC_{RMS} with the following integral over the sample volume:

$$\Delta C_{RMS}^2 = \frac{1}{V}\int [C(r) - \alpha]^2 dV$$

We can use the coarea formula to solve this equation for the interfacial width w. While the case we apply — a simple linear transition — invokes only a very familiar case used in physics calculations, this method will work for a wide range of bounded curvature "cylinders". In the calculation below, ΔC_{RMS}^2 is called the fractional reduction in RMS.

Coarea Formula

While anybody who has taken multivariable calculus has seen Fubini's theorem,[10] in action — we almost always do multivariable integrals one coordinate at a time — usually that deep generalization of this theorem called the coarea (pronounced co-area) formula is not well known outside of geometric analysis.

Recalling Fubini

Recalling Fubini's theorem for the case that

$$\Omega = [a_1, b_1] \times [a_2, b_2] \times [a_3, b_3] \cdots [a_n, b_n] \subset \mathbb{R}^n$$

We have:

$$\int_{\Omega \subset \mathbb{R}^n} g(\vec{x}) d\vec{x} = \int_{a_1}^{b_1} \left(\int_{a_2}^{b_2} \left(\int_{a_3}^{b_3} \cdots \left(\int_{a_n}^{b_n} g(x)\, dx_n \right) \cdots dx_3 \right) dx_2 \right) \cdots dx_1$$

Which, in the case of 2 dimensions becomes:

$$\int_{\Omega \subset \mathbb{R}^2} g(\vec{x}) d\vec{x} = \int_{a_1}^{b_1} \left(\int_{a_2}^{b_2} g(x_1, x_2)\, dx_2 \right) dx_1$$

Fiddling with Representations

Now will do something that might seem a bit overly complicated, but will help us move to the generalization. We define $F(x_1, x_2) = x_1$ We notice that the length of the gradient vector of this map is the constant 1 and note that this is $\sqrt{\det(\nabla F \cdot \nabla F^*)}$ which we call *J F*. (In general, for $F: E \subset \mathbb{R}^n \to \mathbb{R}^k$ where $k \leq n$, $\sqrt{\det(DF \cdot DF^*)}$ where *DF* is the $k \times n$ dimensional matrix

of partial derivatives of *F* and *DF* is its transpose.) We also notice that the first (innermost) iterated integral is the integral over level sets of *F* — i.e. we are integrating over subsets of the domain where the value of *F* (i.e. x_1) is fixed. So far, there is nothing new—we are simply changing representations. Finally, we will write μ to represent the usual area measure on $\mathbb{R}^2$ and $\mathcal{H}^1$ to represent the 1-dimensional length measure on 1-dimensional sets (this is the 1-dimensional Hausdorff measure).

Using our Fiddle to get to the Punchline

Let's rewrite the last integral using these representations:

$$\int_{\Omega \subset \mathbb{R}^2} g(x) J\, F(x) d\mu = \int_{a_1}^{b_1} \left(\int_{F^{-1}(x_1) \cap \Omega} g(x_1, x_2)\ d\mathcal{H}^1 \right) dx_1$$

At this point, it is very important for you to convince yourself that every piece of this makes sense to you for the simple reason that once you have the steps up to the coarea formula is much easier.

Why? *Because*: the coarea formula in our case is given by:

$$\int_E g(x) J\, F d\mu = \int_{\mathbb{R}} \int_{F^{-1}(y) \cap E} g(x) d\mathcal{H}^1(x) dy$$

Where $J\,F$ is the Jacobian of $F\colon \mathbb{R}^2 \to \mathbb{R}$, $\mathcal{H}^1$ is the 1-dimensional Hausdorff measure, and μ is the area measure on $\mathbb{R}^2$.

Now, the slick thing: $F\colon \mathbb{R}^2 \to \mathbb{R}$, $\mathcal{H}^1$ *can be any Lipschitz continuous mapping.*

(Recall that a function is Lipschitz continuous if there is a positive constant $K < \infty$ such that $|F(x) - f(y)| \leq K\,|x - y|$ for every *x*, *y*, in the domain of *F*.)

The picture is that instead of integrating over level sets of F being the planes defined by the equation $F(x_1, x_2) = x_1$ for some fixed x_1, we can integrate over level sets of any Lipschitz function. In our case, we are integrating over the level sets of the distance function to the set = {center of the disk} which coincide with a choice of F = the distance function to the disks of higher density. See Figure S23.

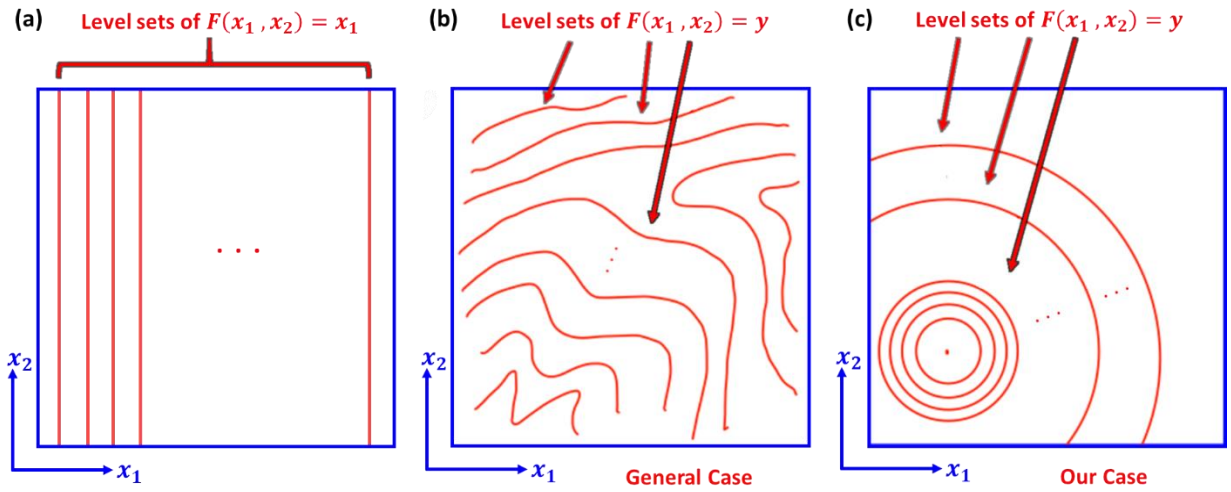

Figure S 24: a) The usual case of Fubini's Theorem. b) The coarea formula is a deep generalization. It applies to wild sets of mappings *F* that are merely Lipschitz continuous. c) Our case—a common one in physics problems with symmetries—is the case in which the level sets are spheres of some dimension.

The Co-area Formula in our Case

Because $J\,F = \sqrt{\det(\nabla F \cdot \nabla F^*)} = 1$ except for a set of measure 0 when F is a distance function, the above formula reduces to:

$$\int_E g(x)\,d\mu = \int_{\mathbb{R}} \int_{F^{-1}(y)\cap E} g(x) d\mathcal{H}^1(x) dy$$

and because we will choose transition functions $g(x)$ which are constant on the level sets of *F*, we can further simplify to:

$$\int_E g(x)\,d\mu = \int_{\mathbb{R}} g(F^{-1}(y))\mathcal{H}^1(F^{-1}(y)\cap E)\,dy$$

where μ now is the area measure on *E*

Two Cases

We now compare the cases in which $g(x) = (C(r)-\alpha)^2$ is either a sharp transition between regions of constant density and the case in which it is a linear transition (See Figures S22b and c).

As a result, we can see that

$$\int_E \left(C(r)-\frac{1}{2}\right)^2 d\mu = \begin{cases} \frac{1}{4}\mu(E) & sharp\ transition \\ <\frac{1}{4}\mu(E) & non-sharp\ transition \end{cases}$$

Assuming a hexagonal arrangement, we get that each equilateral triangle contains $\frac{1}{2}$ disk. So, as long as *E* is some union of these equilateral triangles (see Figure S24), we get that

$$\int_E \left(C(r)-\frac{1}{2}\right)^2 d\mu$$

$$= \frac{1}{4}\mu(E) - N_E\left(\frac{1}{4}\frac{\pi}{2}\left(\left(R+\frac{w}{2}\right)^2-\left(R-\frac{w}{2}\right)^2\right)-\int_{R-\frac{w}{2}}^{R+\frac{w}{2}}\pi r\left(C(r)-\frac{1}{2}\right)^2 dr\right)$$

where the part we have used the coarea formula for is the integral on the right side of the above equation and where

$$N_E = \text{numbers of equilateral triangles in } E$$

and where

$$\left(C(r)-\frac{1}{2}\right)^2 = \left(\frac{R-r}{w}\right)^2$$

Now, if we define d to be the distance between centers, i.e. the characteristic length L_C (See Figure S24b), the area A of one equilateral triangle is

$$A = \frac{\sqrt{3}\mathrm{d}^2}{4}$$

$$\alpha = \frac{A_p}{A} = \frac{2\pi R^2}{\sqrt{3}d^2}$$

$$R = d\sqrt{\frac{\sqrt{3}\alpha}{2\pi}}$$

Where A_p is the polymer area inside the equilateral triangle in Figure S24b, i.e. the area of $\frac{1}{2}$

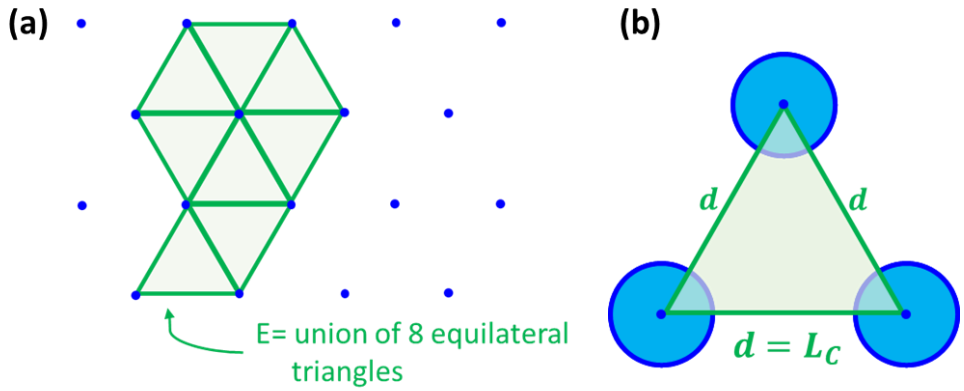

Figure S 25: a) Example of a set E, a union of eight equilateral triangles. b) Basic equilateral formed by centers, where the center-to-center spacing d equals the characteristic length L_C that was measured from RSoXS.

disk.

And we conclude:

$$\int_E \left(C(r) - \frac{1}{2}\right)^2 d\mu = \frac{N_E}{4}\left(\frac{\sqrt{3}d^2}{4} - \pi R w + 4\pi \int_{R-\frac{w}{2}}^{R+\frac{w}{2}} r\left(\frac{R-r}{w}\right)^2 dr\right)$$

Evaluation of the integral is

$$4\pi \int_{R-\frac{w}{2}}^{R+\frac{w}{2}} r\left(\frac{R-r}{w}\right)^2 dr = \frac{1}{3}\pi w R$$

So, continuing:

$$\int_E \left(C(r) - \frac{1}{2}\right)^2 d\mu = \frac{N_E}{4}\left(\frac{\sqrt{3}d^2}{4} - \frac{2}{3}\pi R w\right)$$

and the fractional reduction in RMS compared to the sharp transition is:

$$\Delta C_{RMS}^2 = \frac{\frac{N_E}{4}\left(\frac{\sqrt{3}d^2}{4} - \frac{2}{3}\pi R w\right)}{\frac{N_E}{4}\frac{\sqrt{3}d^2}{4}}$$

$$\Longrightarrow \Delta C_{RMS}^2 = 1 - \frac{8\pi R w}{3\sqrt{3}d^2}$$

Thus, the interfacial width becomes

$$w = \frac{3\sqrt{3}d^2}{8\pi \mathrm{R}}(1 - \Delta C_{RMS}^2)$$

Uneven Fractions

Suppose that you are actually interested in

$$\int_E (C(r) - \alpha)^2 d\mu$$

where $0 < \alpha < 1$ and $\alpha \neq \frac{1}{2}$.

Then, assuming that C inside the disks is 1 and outside is 0 and that $\alpha = \langle C \rangle$ we notice that:

$$\int_E (C(r) - \alpha)^2 d\mu = \int_E \left(\left(C(r) - \frac{1}{2}\right) - \left(\alpha - \frac{1}{2}\right)\right)^2 d\mu$$

$$= \int_E \left(C(r) - \frac{1}{2}\right)^2 d\mu - \mu(E)\left(\alpha - \frac{1}{2}\right)^2$$

Thus, the adjustment yields

$$\Delta C_{RMS}^2 = \frac{1 - 4\left(\alpha - \frac{1}{2}\right)^2 - \frac{8\pi R w}{3\sqrt{3}d^2}}{1 - 4\left(\alpha - \frac{1}{2}\right)^2}$$

$$\Delta C_{RMS}^2 = 1 - \left(\frac{\left(\frac{8\pi R w}{3\sqrt{3}d^2}\right)}{\left(1 - 4\left(\alpha - \frac{1}{2}\right)^2\right)}\right)$$

and the interfacial width is

$$w = \frac{3\sqrt{3}d^2}{8\pi \mathrm{R}}\left(1 - 4\left(\alpha - \frac{1}{2}\right)^2\right)(1 - \Delta C_{RMS}^2)$$

Remarks

1. It is not hard to change the calculation to accommodate arbitrary transition functions instead of the affine (piecewise linear) transition used here, as long as we stick to transitions that are constant on level sets of the distance function to the disks.
2. While the profile of the rods are disks, we can generalize this to any cylinder over a 2-dimensional figure with bounded curvature. (The curvature bound sets limits on how big $\frac{w}{2}$ can be — we would restrict $\frac{w}{2} < \frac{1}{\kappa}$ where κ is the bound on the curvature, then we can use Steiner type formulas to get the areas of the level sets that we need to use the coarea formula.)
3. As long as the $\frac{w}{2}$-neighborhoods of the rods or generalized cylinders don't intersect we can get a similar result for a distribution of different sizes of disks or cylinders, as outlined below.

   A region *E* with some union of these equilateral triangles contains $\left(\frac{\mathcal{H}^2(\mathrm{E})}{\frac{\sqrt{3}}{2}\mathrm{d}^2}\right)$ hexagonal lattice points, where $\mathcal{H}^2(\mathrm{E})$ is the 2-dimensional Hausdorff measure of *E* (the area of *E*).

   If there are *N* disks in region *E,* and the hexagonal close packed lattice can accommodate all the disks (whatever their radii are) such that none of $R + \frac{w}{2}$ disks intersect, then

$$d_N \equiv \left(\frac{\mathcal{H}^2(E)}{N}\frac{2}{\sqrt{3}}\right)^{\frac{1}{2}}$$

   Defining *n(R)* to be the number of disks of radius *R*, we get that the fractional reduction is

$$\int_E \frac{n(R)}{N}\left(1-\frac{8\pi}{3\sqrt{3}}\frac{R}{d_N}\frac{w}{d_N}\right)dR = \frac{1}{\mathcal{H}^2(E)}\int_E \left(C(r)-\frac{1}{2}\right)^2 d\mu$$

$$= \int_E \frac{n(R)}{N}\,dR \; - \frac{8\pi w}{3\sqrt{3}d_N}\int_E \frac{n(R)}{N}\,\frac{R}{d_N}\,dR$$

$$= 1 \; - \frac{8\pi w}{3\sqrt{3}d_N}\int_E \frac{n(R)}{N}\,\frac{R}{d_N}\,dR$$

The first term reduced to 1 implies that $\frac{n(R)}{N}$ is a probability density function. The integral in the second term implies continuous convex of combination of $\frac{R}{d_N}$ over support of *n(R)*.

Recall that "support" of a function is the set on which it is not zero (more precisely, it is the closure of the set on which it is non-zero).

Now, define $\bar{R} \equiv$ mean of *R* under the distribution $\frac{n(R)}{N}$, that means

$$\bar{R} \equiv \int_E \frac{n(R)}{N}\,R\,dR$$

Then the fractional reduction becomes

$$\Delta C_{RMS}^2 = 1 - \frac{8\pi}{3\sqrt{3}}\frac{\bar{R}}{d_N}\frac{w}{d_N}$$

Thus, the interfacial width becomes

$$w = \frac{3\sqrt{3}}{8}\frac{d_N}{\pi}\frac{d_N}{\bar{R}}(1-\Delta C_{RMS}^2)$$

For the case where $0 < \alpha < 1$ and $\alpha \neq \frac{1}{2}$

$$\Delta C_{RMS}^2 = \frac{1-4\left(\alpha-\frac{1}{2}\right)^2 - \frac{8\pi}{3\sqrt{3}}\frac{w}{d_N}\frac{\bar{R}}{d_N}}{1-4\left(\alpha-\frac{1}{2}\right)^2}$$

$$\Delta C_{RMS}^2 = 1 - \left(\frac{\left(\frac{8\pi}{3\sqrt{3}}\frac{w}{d_N}\frac{\bar{R}}{d_N}\right)}{\left(1-4\left(\alpha-\frac{1}{2}\right)^2\right)}\right)$$

and the interfacial width is

$$w = \left(\frac{3\sqrt{3}}{8}\frac{d_N}{\pi}\frac{d_N}{\bar{R}}\right)\left(1 - 4\left(\alpha - \frac{1}{2}\right)^2\right)(1 - \Delta C_{RMS}^2)$$

Thus, we conclude that even if the radii are not all the same, we can—under the conditions set out above— simply replace R with $\bar{R}$ in the final equation of "fractional reduction" in the constant disk size case.

Blend (NT812:PC71BM)	**NT812 (*Volume Fraction*)**	**PC71BM (*Volume Fraction*)**	***Lc = d* [nm]**	**Equilateral Triangle *Area* (A) [nm²]**	**NT812 Disk *Area* [nm²]**	**NT812 Disk *Radius* (R) [nm]**	**D-A Interfacial *Width* (w) [nm]**
(3:1)	0.77	0.23	62.8	1709.5	2632.6	29.0	7.5 ± 0.9
(3:1) w/CN	0.77	0.23	62.8	1709.5	2632.6	29.0	4.9 ± 0.6
(1:1.5)	0.43	0.57	98.2	4173.5	3589.2	33.8	12 ± 0.3
(1:1.5) w/CN	0.43	0.57	98.2	4173.5	3589.2	33.8	6.7 ± 0.2

Table S 3: Summary of the calculated variables via the donor-acceptor interfacial width calculation. The volume fraction values and characteristic length L_C are from RSoXS analysis.

S 11. RSoXS and GIWAXS: Thickness Comparison

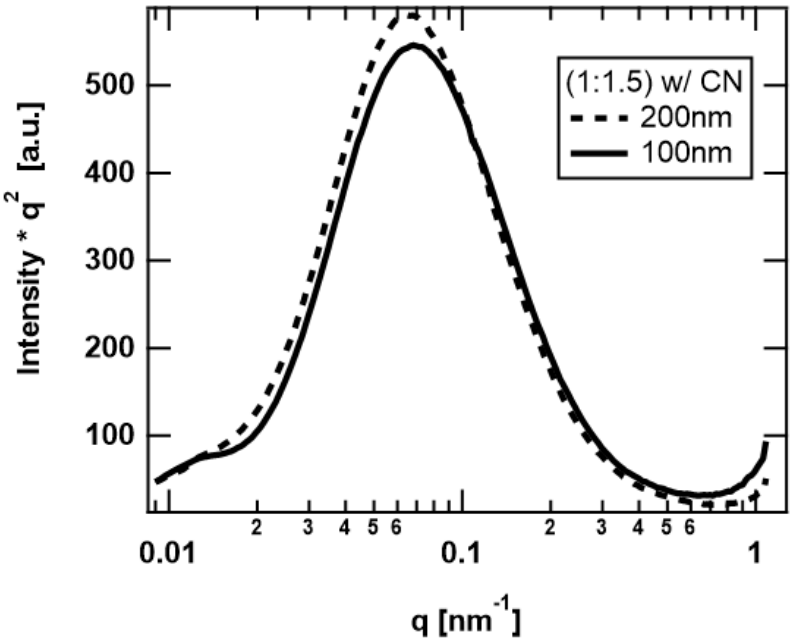

Figure S 26: RSoXS profiles for 1:1.5 blends with CN. The solid profile is for a 100 nm thick blend and dashed for a 200 nm thick film. The results are very similar, suggesting that the composition variation and characteristic length are almost thickness independent.

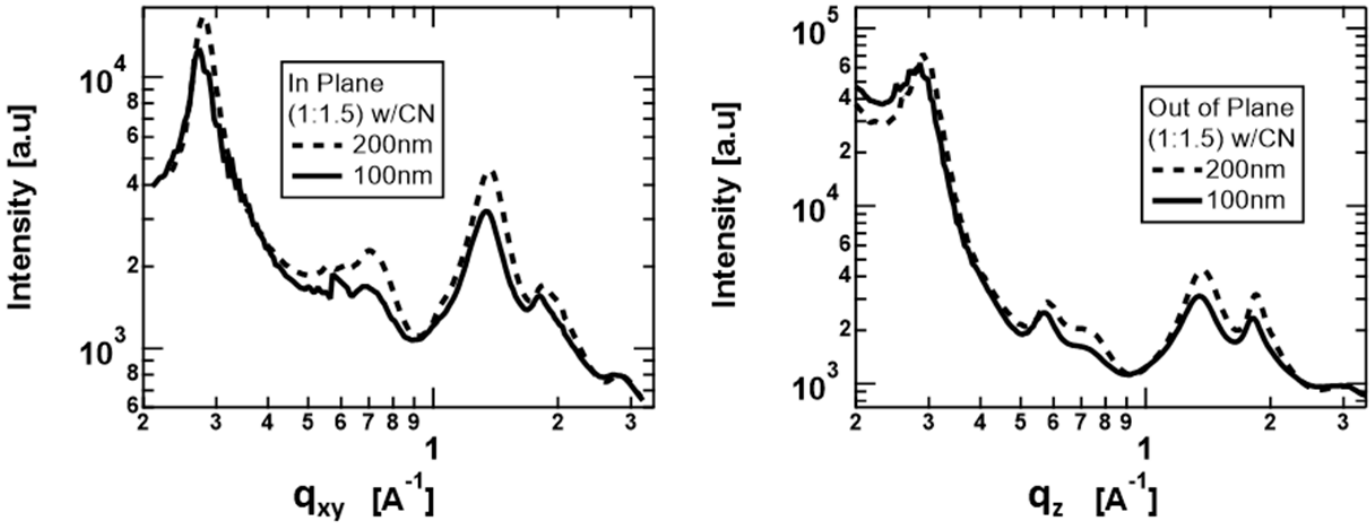

Figure S 27: 1D GIWAXS profiles for 1:1.5 with CN blends with different thickness: 100 nm (solid) and 200 nm (dashed). In plane (left) and out of plane (right). The thinner sample shows lower peak intensities as expected. Otherwise, the results are similar, indicating similar packing and crystallinity in those blends.

S 12. Supporting Information References

(1) Jin, Y.; Chen, Z.; Dong, S.; Zheng, N.; Ying, L.; Jiang, X.-F.; Liu, F.; Huang, F.; Cao, Y. A Novel Naphtho[1,2- *c* :5,6- *C′*]Bis([1,2,5]Thiadiazole)-Based Narrow-Bandgap π-Conjugated Polymer with Power Conversion Efficiency Over 10%. *Adv. Mater.* **2016**, *28* (44), 9811–9818. https://doi.org/10.1002/adma.201603178.

(2) Armin, A.; Chen, Z.; Jin, Y.; Zhang, K.; Huang, F.; Shoaee, S. A Shockley-Type Polymer: Fullerene Solar Cell. *Adv. Energy Mater.* **2018**, *8* (7), 1701450. https://doi.org/10.1002/aenm.201701450.

(3) Hosseini, S. M.; Roland, S.; Kurpiers, J.; Chen, Z.; Zhang, K.; Huang, F.; Armin, A.; Neher, D.; Shoaee, S. Impact of Bimolecular Recombination on the Fill Factor of Fullerene and Nonfullerene-Based Solar Cells: A Comparative Study of Charge Generation and Extraction. *J. Phys. Chem. C* **2019**, *123* (11), 6823–6830. https://doi.org/10.1021/acs.jpcc.8b11669.

(4) Baker, J. L.; Jimison, L. H.; Mannsfeld, S.; Volkman, S.; Yin, S.; Subramanian, V.; Salleo, A.; Alivisatos, A. P.; Toney, M. F. Quantification of Thin Film Crystallographic Orientation Using X-Ray Diffraction with an Area Detector. *Langmuir* **2010**, *26* (11), 9146–9151. https://doi.org/10.1021/la904840q.

(5) Alqahtani, O.; Babics, M.; Gorenflot, J.; Savikhin, V.; Ferron, T.; Balawi, A. H.; Paulke, A.; Kan, Z.; Pope, M.; Clulow, A. J.; Wolf, J.; Burn, P. L.; Gentle, I. R.; Neher, D.; Toney, M. F.; Laquai, F.; Beaujuge, P. M.; Collins, B. A. Mixed Domains Enhance Charge Generation and Extraction in Bulk-Heterojunction Solar Cells with Small-Molecule Donors. *Adv. Energy Mater.* **2018**, *8* (19), 1702941. https://doi.org/10.1002/aenm.201702941.

(6) Burke, K. B.; Luber, E. J.; Holmes, N. P.; Murray, A. J.; Belcher, W. J.; Zhou, X.; Mitlin, D.; Dastoor, P. C. A Knife-Edge Measurement of the Beam Profile of STXM 5.3.2.2 Using a Focussed Ion Beam Milled Metallic Glass. *Journal of Electron Spectroscopy and Related Phenomena* **2012**, *185* (11), 453–457. https://doi.org/10.1016/j.elspec.2012.07.003.

(7) Yan, H.; Wang, C.; McCarn, A. R.; Ade, H. Accurate and Facile Determination of the Index of Refraction of Organic Thin Films Near the Carbon 1 s Absorption Edge. *Phys. Rev. Lett.* **2013**, *110* (17), 177401. https://doi.org/10.1103/PhysRevLett.110.177401.

(8) Collins, B. A.; Ade, H. Quantitative Compositional Analysis of Organic Thin Films Using Transmission NEXAFS Spectroscopy in an X-Ray Microscope. *Journal of Electron Spectroscopy and Related Phenomena* **2012**, *185* (5–7), 119–128. https://doi.org/10.1016/j.elspec.2012.05.002.

(9) Ferron, T.; Pope, M.; Collins, B. A. Spectral Analysis for Resonant Soft X-Ray Scattering Enables Measurement of Interfacial Width in 3D Organic Nanostructures. *Phys. Rev. Lett.* **2017**, *119* (16), 167801. https://doi.org/10.1103/PhysRevLett.119.167801.

(10) Morgan, F. *Geometric Measure Theory: A Beginner's Guide*, 4th ed.; Academic Press/Elsevier: Amsterdam ; Burlington, MA, 2009.